Preprint Cambridge Centre for Computational Chemical Engineering ISSN 1473 – 4273

Lifting an object buried in granular material; experiments and theory

Jethro Akroyd[1,2], Eric J. Rees[1],
Chung Ting Lao[1], Andi Reci[1],
Oscar Maynard[1], Marcus Clover[1],
Ray Aun Fan[1], Khoon Kheng Teh[1],
John F. Davidson[1]

released: July 19, 2019

[1] Department of Chemical Engineering
and Biotechnology
University of Cambridge
Philippa Fawcett Drive
Cambridge, CB3 0AS
United Kingdom

[2] CARES
Cambridge Centre for Advanced
Research and Education in Singapore
1 Create Way
CREATE Tower, #05-05
Singapore, 138602

Preprint No. 232

Keywords: buried plate, uplift force, slip plane, granular material, particle tracking, failure mode

Edited by
Computational Modelling Group
Department of Chemical Engineering and Biotechnology
University of Cambridge
Philippa Fawcett Drive
Cambridge CB3 0AS
United Kingdom

E-Mail: c4e@cam.ac.uk
World Wide Web: http://como.ceb.cam.ac.uk/

Abstract

The paper describes experiments and theory relating to particle movements when a horizontal plate, buried in granular material, is lifted. The experiments were quasi two-dimensional. Glass ballotini were contained between two vertical glass plates separated by a distance of 24 mm. A buried horizontal rectangular plate, 24 mm $\times$ 45 or 60 mm was lifted vertically, giving two slip planes starting from the edges of the plate; the slip planes were inclined at angles $\pm\alpha$ to the vertical. The measured lift force increased steeply with upward displacement, reaching a maximum after a small displacement. Further movement caused a fall in lift force, as observed by many authors. A novelty in this work was to measure the motion of individual particles: the movements showed clearly that near the vertical centre line, there was 'active' failure, i.e. (vertical stress) $>$ (horizontal stress). Near the failure surfaces, at angles $\pm\alpha$ to the vertical, there was 'passive' failure. Outside the failure zones the stresses were isotropic (equal stresses vertically and horizontally). On the basis of these observations, the 'reverse hopper' theory was developed; the theory assumes active failure near the vertical centre line. It predicts the dimensionless peak lift force N_{qf} and the angle α, in reasonable agreement with the rather scattered data from the experiments. The existence of well-defined slip planes is equivocal, as suggested by the experimental techniques employed, as follows:

(i) A photographic technique registered black for a particle that moved more than a threshold quantity; particles with smaller movements registered white. Results show clearly defined slip planes.

(ii) Observations of individual particles showed movement profiles with significant movement in the middle of the failure zone, but falling off gradually with distance from the vertical centre line. This suggests that the existence of slip planes is equivocal; a threshold value of particle movement had to be identified to define a slip plane.

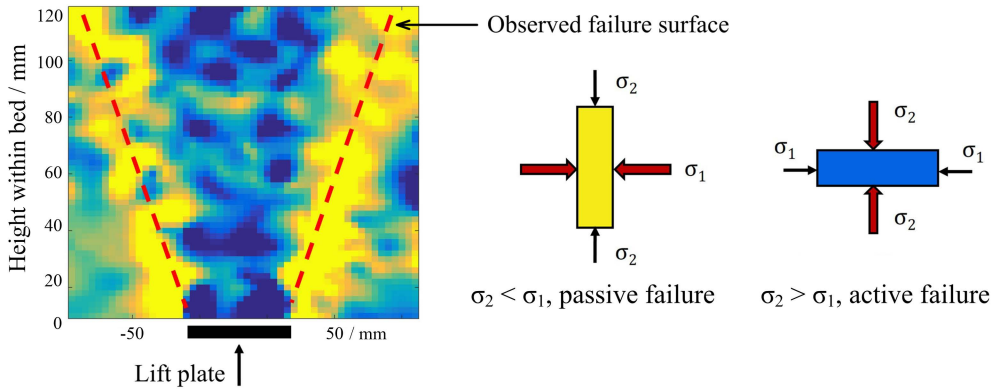

Highlights

- Experiments performed on ballotini contained between two vertical glass plates.
- Force to lift a buried horizontal plate measured as a function of displacement.
- Particle imaging used to observe slip planes and failure mode of ballotini.
- Passive failure near slip planes; active failure between slip planes.
- Reverse Hopper Theory predicts uplift force and angle of slip planes.

Contents

1 Introduction

The force required to lift an object buried in granular material is relevant to the design of anchors for ships or oil rigs. It is also relevant to the stability of buried pipelines, which may experience compressive thrusts promoting buckling, which may occur if the pipe burial is too shallow. The similarity of such pipe lifts was noted by Dickin [5] and by Cheuk et al. [2]. Similarity to full-scale conditions was achieved by Dickin [4] using centrifuge testing, see also Moradi and Craig [17]. But it appears that industrial design of anchors is empirical, see Merifield and Sloan [15].

The paper presents results about the force needed to lift a horizontal rectangular plate buried in granular material. The work was quasi two-dimensional: the glass ballotini were contained between two vertical parallel plates separated by a horizontal distance of 24 mm, so that particle motion could be observed. Superficial observations suggest the existence of two slip planes, starting at each edge of the horizontal lift plate and inclined at an angle $\pm\alpha$ to the vertical. Thus the bed above the plate appears to consist of two regions:

(i) A moving core, between the slip planes.

(ii) Two stationary regions outside the slip planes.

On the basis of these simple observations, theory is presented to predict α, and also F_{T}, the peak force to lift the plate. The actual particle movements were revealed by particle tracking experiments as follows. The movement of black ballotini admixed to make up approximately 1% of the granular material was observed by photography: by taking two photographs, separated by a short time interval, the direction of motion was inferred. Also, by particle tracking, the motion of an initially square array of the material could be identified, and it could be determined whether the distortion of each square implied active or passive failure. The theory gives moderately good agreement with the rather scattered experimental results. The differences between theory and experiment are probably due to movement of the particles being more complex than what is described above.

2 Literature Review

The substantial literature on the uplift of an object buried in granular material will be discussed by reference to:

(i) Experimental techniques.

(ii) Lift force in relation to vertical displacement.

(iii) Shapes of failure surfaces.

(iv) Theoretical analysis.

(v) Practical applications.

2.1 Experimental techniques

Most researchers used laboratory-scale equipment instead of full-scale experiments which are costly [26]. A variety of arrangements was used to give uplift *e.g.* a hydraulic jack [16], or a motor and gearbox [2, 5]. Particle movement was observed using coloured sand [26, 30]. Particle image velocimetry [2, 30] gave particle velocity and particle displacement.

2.2 Relation between lift force and displacement

Fig. 1, below, shows the relation between lift force and displacement. Many authors have made similar observations, *i.e.* that the force to lift the plate in the granular material first increases steeply with plate displacement (a), reaching a peak force F_T after a relatively small displacement. Further plate movement gives a fall in lift force (b), decreasing gradually with further upward movement of the plate (c). It is usual to report the breakout factor $N_{qf} = \frac{F_T}{\rho g H D w}$ where F_T is the peak lift force, ρ is the bulk density of the lifted particles, H is the bed depth, D is the plate width, w is the distance between the two vertical plates retaining the bed, and g is the acceleration due to gravity. Thus N_{qf} = (Peak lift force)/(weight of granules directly above the lift plate); this applies for rectangular plates, as here, or for circular plates.

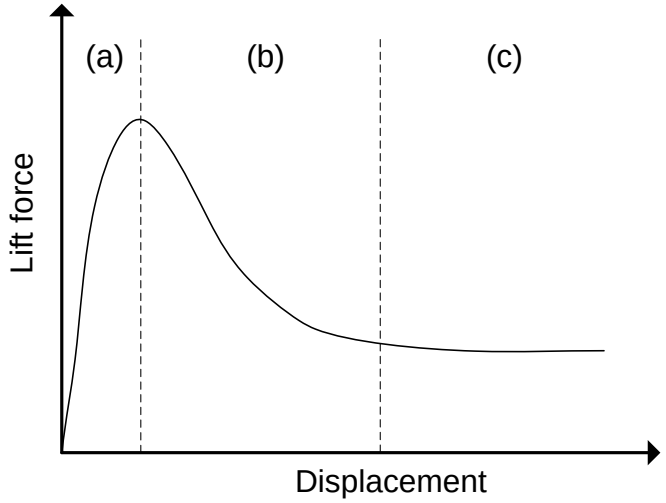

Figure 1: *Typical relationship between lift force and displacement, with three different phases indicated in the figure. Adapted from Lee et al. [10].*

2.3 Shapes of failure surfaces

When the plate, or other object immersed in the granular material, is lifted, a body of granules above the plate is also lifted. Many authors have identified a failure surface, the boundary between the moving granules and the stationary granules outside; this boundary is assumed, or observed, to take one of the following alternative shapes shown in Fig. 2:

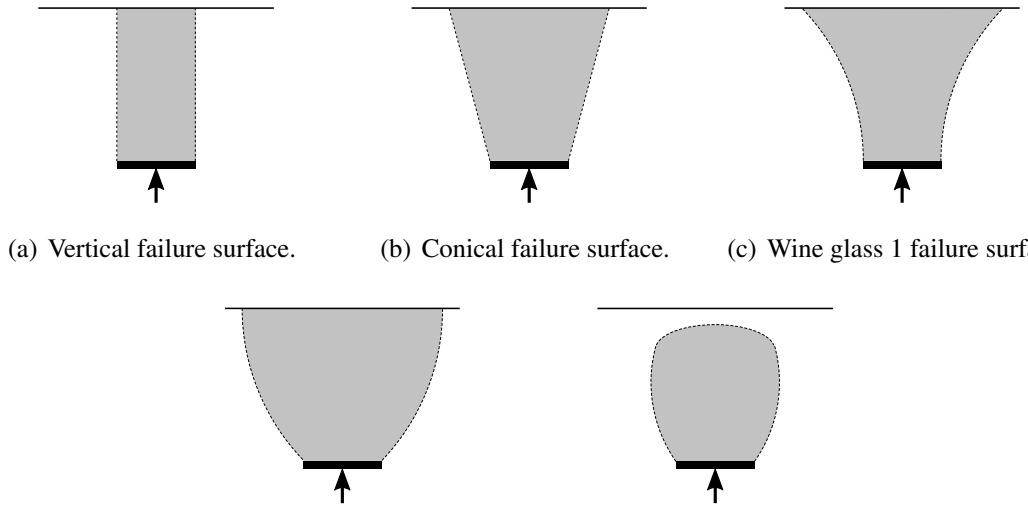

(a) Vertical failure surface. (b) Conical failure surface. (c) Wine glass 1 failure surface.

(d) Wine glass 2 failure surface. (e) Balloon failure surface.

Figure 2: *Various failure surfaces proposed and observed in the literature.*

(i) Vertical, Fig. 2(a). Here the failure is assumed to be on vertical lines emanating from the edges of the lift plate. Thus the failure surface is assumed to be

   (a) a vertical cylinder for a circular lift plate or

   (b) a finite width slab for a two-dimensional bed between vertical retaining plates.

(ii) Conical, Fig. 2(b). Here the failure surface is two straight lines, emanating from the edges of the lift plate and inclined at angle α to the vertical. Thus the failure surface is a cone of half angle α for a circular lift plate; for a 'two-dimensional' system, the failure surface is two flat surfaces starting from the edges of the plate, each surface inclined at angle α to the vertical. This assumption has been used by many authors, and is the basis of the theoretical work in this paper.

(iii) Wine glass 1, Fig. 2(c). Some authors have reported a failure surface whose inclination to the vertical increases with vertical distance above lift plate. In the axi-asymmetric case, the surface resembles that of some wine glasses.

(iv) Wine glass 2, Fig. 2(d). Here the inclination to the vertical diminishes with distance above the lift plate. In the axi-symmetric case, this surface resembles that of more conventional wine glasses: at the top, the surface is nearly vertical.

(v) Balloon shape, Fig. 2(e). For a deeply immersed plate, the failure surface may not extend to the horizontal top surface of the granule bed. For an axi-symmetric system, the failure surface is of 'balloon' shape, perhaps with a flat top which is below the top surface of the granule bed.

Publications on the shapes of failure surfaces are as follows. Majer [12], Mors [18], Balla [1], MacDonald [11], Matyas and Davis [13], Dickin [4], Ghaly et al. [7], Rao and Kumar [23], Ilamparuthi et al. [8], Cheuk et al. [2], White et al. [31], Lee et al. [10].

2.4 Theoretical analysis

A variety of theoretical analyses have been published. Finite element analysis was used by Rowe and Davis [25] and by Merifield and Sloan [15]. Authors have made a variety of assumptions as to the form of the slip surface between the moving granules around a centreline [4, 11, 12, 15, 18, 19, 21, 28, 29, 31]. Lee et al. [10] postulated that the lift force is the sum of the weight of displaced material and the shear forces at the slip surface; this hypothesis is used in this paper.

3 Theory to predict the uplift force and failure angle

Fig. 3 shows the assumed motion induced by lifting particles resting on a flat plate of width D. The particles are contained between two vertical glass plates separated by a distance w.

These glass plates are parallel to the plane of the diagram shown in Fig. 3. It is assumed that the material is a cohesionless Coulomb material and that there are two well defined slip planes inclined at angle α to the vertical; each plane is a boundary between stationary and moving material. Between the slip planes, active upward motion is assumed. The principal stresses, σ_1 and σ_2 are shown in Fig. 3; $\sigma_2 > \sigma_1$. As an element is pushed up, its height diminishes and its width increases, indicating active failure as assumed by Lee et al. [10], who gave an analysis to predict σ_1 and σ_2 as a function of the radius r. From their Equation (21),

$$\sigma_2 = \frac{K\rho g r}{2K-1}\left[\left(\frac{r_1}{r}\right)^{\left(2-\frac{1}{K}\right)} - 1\right]. \tag{1}$$

Here ρ is the bulk density of the granules and g is the acceleration due to gravity; the radii r and r_1 are shown in Fig. 3 and K is the Rankine coefficient of earth pressure,

$$K = \frac{\sigma_2}{\sigma_1} = \frac{1+\sin\phi}{1-\sin\phi}. \tag{2}$$

Equation (2) is based on Mohr's circle (Nedderman [20], Chapter 3). The internal friction angle of the granules, ϕ, can be derived from $\tan\phi = \mu$, where μ is the friction coefficient of the granular material.

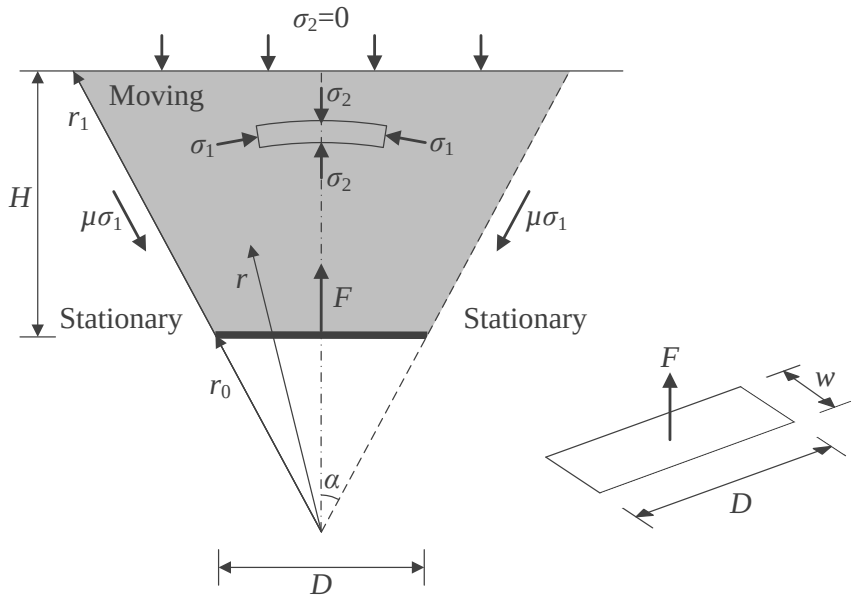

Figure 3: *Stresses in flowing granular material when an upward force F is applied to a buried plate of width D. The grey area represents moving granular material. The isometric view of the lift plate shows the distance w between the vertical glass plates containing the granules; D is the plate width. Adapted from Clover [3].*

3.1 Break-out factor

Experiments show that as the plate is lifted, the lift force F reaches a maximum F_T after small upward displacement [2]. We define the break-out factor

$$N_\mathrm{qf} = \frac{F_\mathrm{T}}{\rho g H D w}, \tag{3}$$

which is a dimensionless form of F_T. The dimensions H and D are shown in Fig. 3 where w is the distance between the vertical glass plates. Lee et al. [10] derive an equation for the break-out factor by consideration of the vertical and shear components of σ_1 and σ_2. Using Equation (30) from Lee et al. [10], with our D in place of their B gives

$$\begin{aligned} N_\mathrm{qf} = {} & \frac{DK}{2H\,(2K-1)\sin\alpha}\left[\zeta^{\left(2-\frac{1}{K}\right)}-1\right] \\ & + \frac{\mu D\cos\alpha}{2H\,(2K_\mathrm{f}-1)\sin^2\alpha}\left[\left(K_\mathrm{f}-\frac{1}{2}\right)\zeta^2 - K_\mathrm{f}\,\zeta^{\left(2-\frac{1}{K_\mathrm{f}}\right)}+\frac{1}{2}\right], \end{aligned} \tag{4}$$

where $\zeta = 1 + \frac{2H\tan\alpha}{D}$ and where we introduce K_f to denote the terms in K arising from the shear stress at the failure surface between the moving and stationary material. It is assumed that the material in the failure surface is in passive failure (see Nedderman [20], Chapter 3), such that $K_\mathrm{f} = 1/K$. Note also that the term containing μ in Equation (4) is equivocal, see Lee et al. [10].

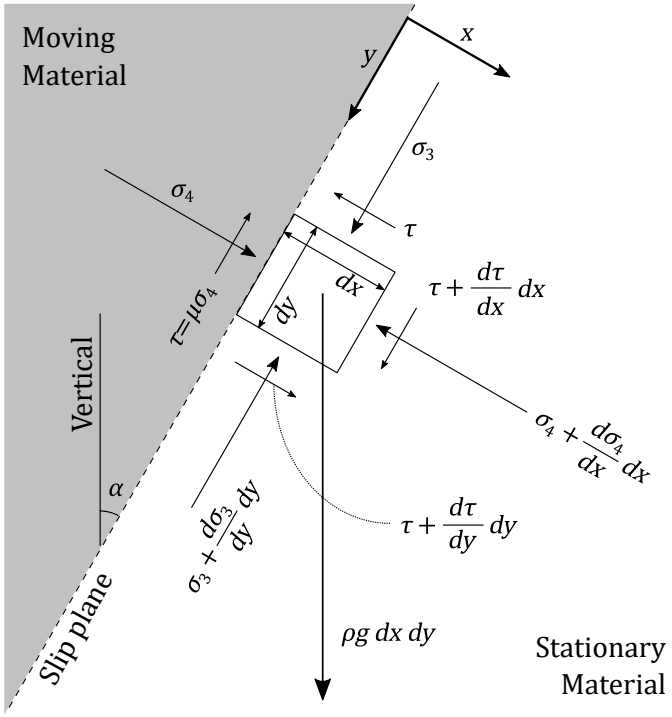

Figure 4: *Stress distribution for a stationary element adjacent to slip plane.*

As shown in Fig. 4, it is assumed that there is a shear stress of $\tau = \mu\sigma_4$ at the interface between stationary and moving granules, inconsistent with the supposition that σ_1 is a principal stress. But this indefensible assumption gives, as shown by Lee et al. [10], good agreement between theory and experiment for F_T.

3.2 Determination of slip angle

Fig. 4 shows the forces on a stationary element just outside the slip plane. Resolving in direction y, Fig. 4, gives

$$\frac{d\sigma_3}{dy} = \rho g \cos\alpha + \frac{d\tau}{dx}. \tag{5}$$

Resolving in direction x, Fig. 4, gives

$$\frac{d\sigma_4}{dx} = \rho g \sin\alpha + \frac{d\tau}{dy}. \tag{6}$$

Using the above mentioned approximation, i.e. $\tau = \mu\sigma_4$ gives, from Equation (6)

$$\frac{1}{\mu}\frac{d\tau}{dx} = \rho g \sin\alpha + \mu\frac{d\sigma_4}{dy},$$

and eliminating $\frac{d\tau}{dx}$, using Equation (5), gives

$$\frac{d\sigma_3}{dy} = \rho g\,(\cos\alpha + \mu\sin\alpha) + \mu^2\frac{d\sigma_4}{dy}. \tag{7}$$

Now we need to make an assumption about the stress regime in the stationary material: there are three possibilities, namely:

$$\text{(1) Active failure,} \qquad \sigma_3 = K\sigma_4. \tag{8a}$$

$$\text{(2) Isotropic behaviour,} \qquad \sigma_3 = \sigma_4. \tag{8b}$$

$$\text{(3) Passive failure,} \qquad \sigma_4 = K\sigma_3. \tag{8c}$$

We choose option (2) i.e. isotropic behaviour. This is plausible because the stationary material is not moving. Also, analyses by Clover [3], Fan [6], Teh [27] and Maynard [14] suggest that the isotropic assumption gives the best agreement between theory and experiment. Combining Equations (7) and (8b) gives

$$\frac{d\sigma_4}{dy}\left(1-\mu^2\right) = \rho g\left(\cos\alpha + \mu\sin\alpha\right). \tag{9}$$

By differentiating Equation (1) with respect to r, we can obtain

$$\frac{d\sigma_2}{dr} = -\frac{K\rho g}{2K-1}\left[\left(1-\frac{1}{K}\right)\left(\frac{r_1}{r}\right)^{\left(2-\frac{1}{K}\right)}+1\right]. \tag{10}$$

For equilibrium at the slip plane, $\sigma_4 = \sigma_1$. Equation (10) can be substituted into Equation (9) by the following coordinate transformation

$$\frac{d\sigma_4}{dy} = -\frac{d\sigma_1}{dr} = -\frac{1}{K}\frac{d\sigma_2}{dr}, \tag{11}$$

since the moving region is assumed to be in active failure. In order to obtain the value of α near the lift plate, the most important region, $r = r_0$ is used. It can be derived from Fig. 3 that $H = (r_1 - r_0)\cos\alpha$ which leads to $\frac{r_1}{r_0} = 1 + \frac{2H\tan\alpha}{D}$. The resulting equation for α is therefore

$$\frac{1-\mu^2}{2K-1}\left[\left(1-\frac{1}{K}\right)\zeta^{\left(2-\frac{1}{K}\right)}+1\right] = \cos\alpha + \mu\sin\alpha, \tag{12}$$

where $\zeta = 1 + \frac{2H\tan\alpha}{D}$.

4 Equipment and Measurements

Fig. 5 shows equipment for studying the flow of granular material [3, 6, 9, 14, 24, 27], upwards or downwards, and either

(i) between two vertical glass plates, separated by a distance of 24 mm, see Fig. 5 (b), or

(ii) downwards or upwards flow through a semi-circular cylindrical hopper, see Fig. 5 (b), giving axi-symmetric flow, visible through the two glass plates, see Fig. 5 (b).

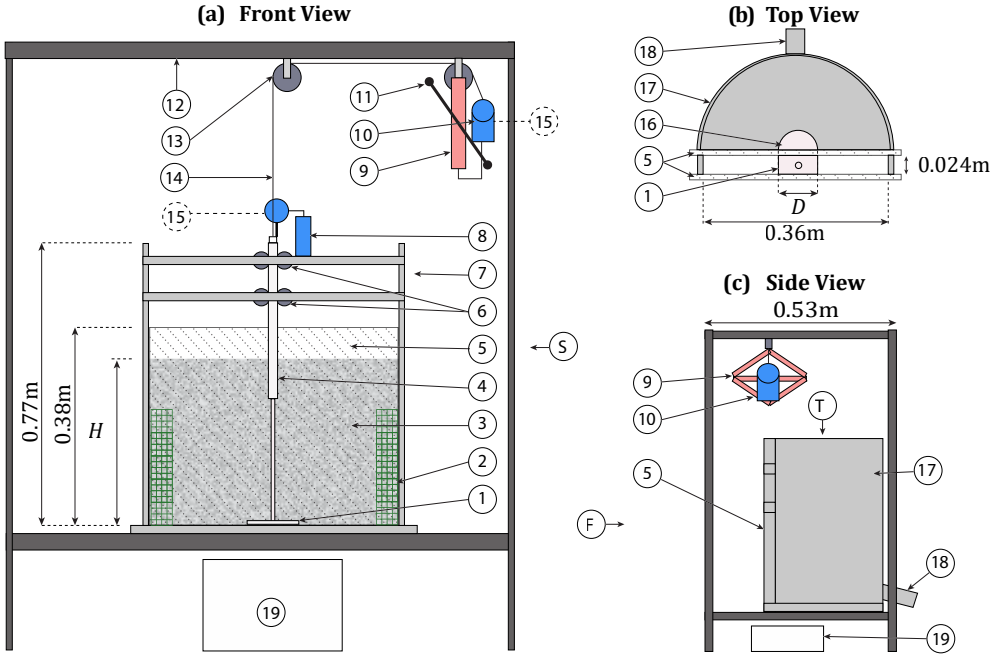

Figure 5: *Equipment, not to scale, from Fan [6]. Numbered items are as follows: 1. Plate for lifting; 2. Grid paper; 3. Ballotini; 4. Lifting rod; 5. Parallel glass plates; 6. Rollers; 7. Support frame; 8. Displacement gauge; 9. Scissor jack; 10. Force gauge; 11. Jack; 12. Support frame; 13. Pulley; 14. Flexible wire; 15. Signal to computer; 16. Semi-circular plate (not used in this work); 17. Semi-circular container; 18. Nozzle to empty equipment; 19. Collection container.*

Here we are concerned only with two-dimensional flow between the two glass plates shown in Fig. 5 (b).

The glass ballotini are shown as Item 3 in Fig. 5 (a), a view seen looking in a horizontal direction normal to the glass plates. Here we deal with the upward movement of a flat horizontal plate, Item 1 in Fig. 5, (a) and (b), 24 mm wide, with values of D = 45 or 60 mm. Thus two lift plates were employed, each lifted by a vertical rod, Item 4 in Fig. 5 (a). Fig. 5 shows the arrangement of wire and pulleys to lift the plate through the granular material. The lift force and the plate displacement were measured, with a constant rate of displacement and a progressively increasing lift force and displacement, while observing the movement of the granular material through the front glass plate.

4.1 Properties of the ballotini

Table 1 shows the properties of the ballotini used in the experiments. The similarity of the friction angles showed that the relation between shear stress and shear strain was similar for types A, B and C.

Properties of the ballotini						
Type	Diameter	Solid density	Bulk density		Friction angle	
			Untapped	Tapped	Untapped	Tapped
	mm	kg m^{-3}	kg m^{-3}	kg m^{-3}	degrees	degrees
A	2.9 ± 0.2	2900	1900 ± 20	1910 ± 20	30.5	36.9
B	1.0 ± 0.1	2760	1710 ± 20	1730 ± 20	29.8	41.7
C	0.37 ± 0.08	2460	1520 ± 20	1560 ± 20	28.8	34.6

Table 1: *The properties of the three types of ballotini used in the experiments. measured by Reci [24] and Lao [9] with a normal stress of 100 kPa (10 m water gauge).*

4.2 Contribution of wall friction to the measured break-out factor

In addition to the contributions considered in Section 3.1, the uplift force and therefore break-out factor measured in the experiments is subject to a contribution from the friction between the ballotini and the glass plates of the equipment as shown in Fig. 5 (b).

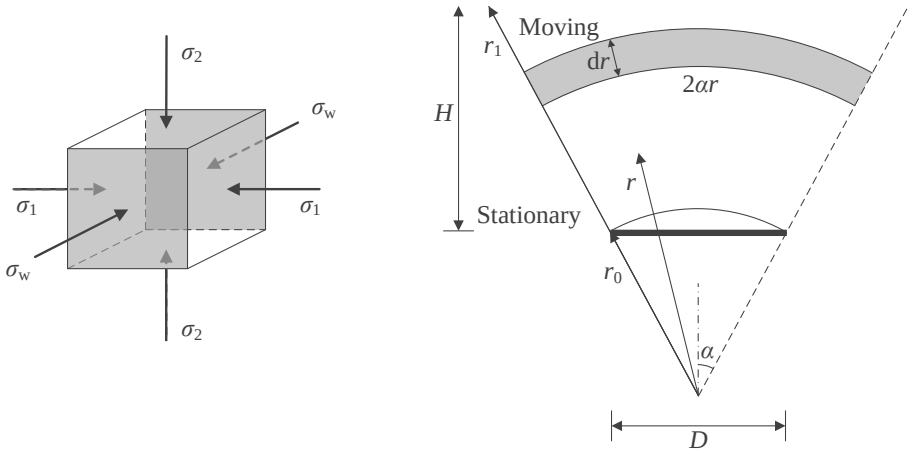

Figure 6: *Normal stresses acting on an element in the bed (left). The shaded regions represent the glass walls of the apparatus. A radial strip (shaded) of width dr (right), used in the calculation of the wall friction.*

Fig. 6 shows the normal stresses acting on an element of the bed. The ballotini are assumed to be isotropic so that the material properties are identical in all directions. With this assumption, the strain perpendicular to the wall, ε_w, is related to the stresses shown in Fig. 6 by a generalised Hooke's law

$$\varepsilon_w = \frac{1}{E}\left(\sigma_w - \nu\left(\sigma_1 + \sigma_2\right)\right), \tag{13}$$

where E is the Young modulus and ν is the Poisson ratio of the ballotini, assumed to be 0.3 which is typical for sand and gravels [22]. The ballotini are constrained by the rigid

glass walls such that $\varepsilon_w = 0$. Equation (13) can therefore be simplified to give

$$\sigma_w = \nu\,(\sigma_1 + \sigma_2)\,. \tag{14}$$

The frictional force due to the stress on the walls is estimated as

$$F_w = 2\mu_w \int_{r_0}^{r_1} \sigma_w\, 2\alpha r\, \mathrm{d}r, \tag{15}$$

where μ_w is the coefficient of friction between the ballotini and the glass walls and $2\alpha r\,\mathrm{d}r$ is the area of the shaded strip shown in Fig. 6. An additional factor of 2 is included because there are two glass plates in contact with the ballotini. Using Equation (14) to substitute σ_w and the expressions for σ_1 and σ_2 in Equations (1) and (2), Equation (15) can be solved to give

$$F_w = \frac{4\rho g}{3}\,\frac{\alpha\mu_w\nu}{2K-1}{r_0}^3\left[1-\zeta^3+K\left(1+2\zeta^3-3\zeta^{\left(2-\frac{1}{K}\right)}\right)\right], \tag{16}$$

where $\zeta = \frac{r_1}{r_0} = 1 + \frac{2H\tan\alpha}{D}$. The corresponding contribution to the observed break-out factor is given

$$N_{\mathrm{qf}_w} = \frac{F_w}{\rho g H D w},$$

and using Equation (16) gives

$$N_{\mathrm{qf}_w} = \frac{D^2}{6Hw}\,\frac{\alpha\mu_w\nu}{2K-1}\left(\frac{1}{\sin\alpha}\right)^3\left[1-\zeta^3+K\left(1+2\zeta^3-3\zeta^{\left(2-\frac{1}{K}\right)}\right)\right]. \tag{17}$$

4.3 Particle tracking

In addition to measuring the force to lift the plate and the plate displacement, the movements of individual particles were measured from photographs [6, 27]. The bed particles were mainly transparent glass ballotini, but a small proportion of black ballotini was added, so that the motion of individual particles could be tracked.

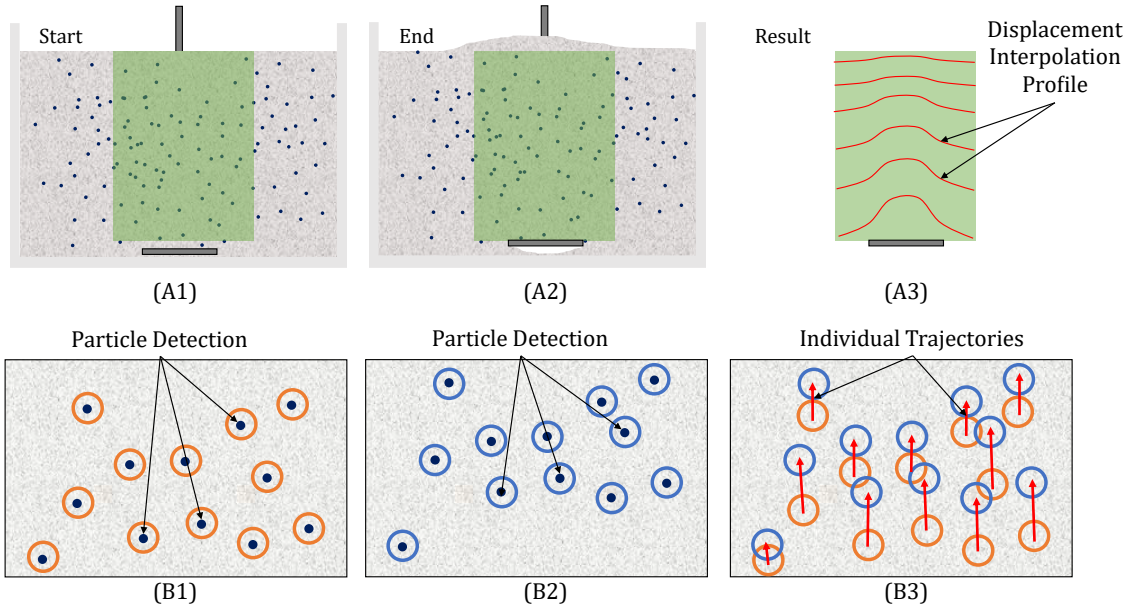

Figure 7: *Particle tracking: (A1) and (A2) show how the marked particles were photographed; (A3) shows displacement profiles; (B1) and (B2) show particle detection at the start and finish, giving trajectories in (B3). From Fan [6].*

Fig. 7 demonstrates the particle tracking method. The initial and final position of the tracked particles are shown as B1 and B2 in Fig. 7, giving the trajectories in B3. This allowed the calculation of the displacement profiles as shown in Fig. 7, A3. Grid paper (Item 2 in Fig. 5) was used as a scale bar to enable the calculation of the physical displacement of each particle. See Fig. 7, B3.

4.4 Brightness threshold

An alternative procedure was adopted by Clover [3] and Maynard [14]. In this case all the glass ballotini were transparent. An image-difference was calculated between photographs taken during uplift. This showed which particles had moved and which remained stationary: moving particles caused large differences in image brightness, shown as black regions in Fig. 8. This gave a clearly defined boundary between moved and stationary particles and hence the angle α.

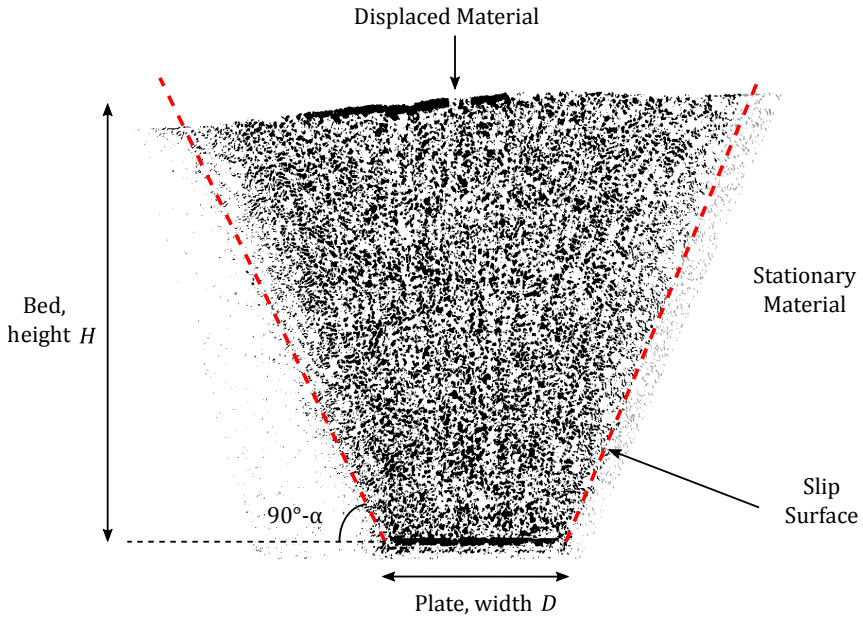

Figure 8: *Detection of slip surface using the brightness threshold algorithm (Clover [3], Maynard [14]).The material is photographed before and after plate movement: the region with moving particles exhibits large changes in image brightness, visualised here as black regions; static material exhibits unchanged image brightness, visualised here as white regions.*

5 Results

5.1 Uplift force

Fig. 9 shows how uplift force varies with displacement of the lift plate. This has a characteristic maximum; prior to the maximum, the displacements are very small, about 2 – 3 mm. At higher displacements, the lift force diminishes. This behaviour is commonly observed in uplift experiments [2, 8]. It is assumed that the maximum uplift force is important, and therefore it is compared with the theoretical prediction developed in Section 3. Based on Fig. 9, it can be concluded that the peak force is not affected by the lift speed providing that the speed of the plate is sufficiently low.

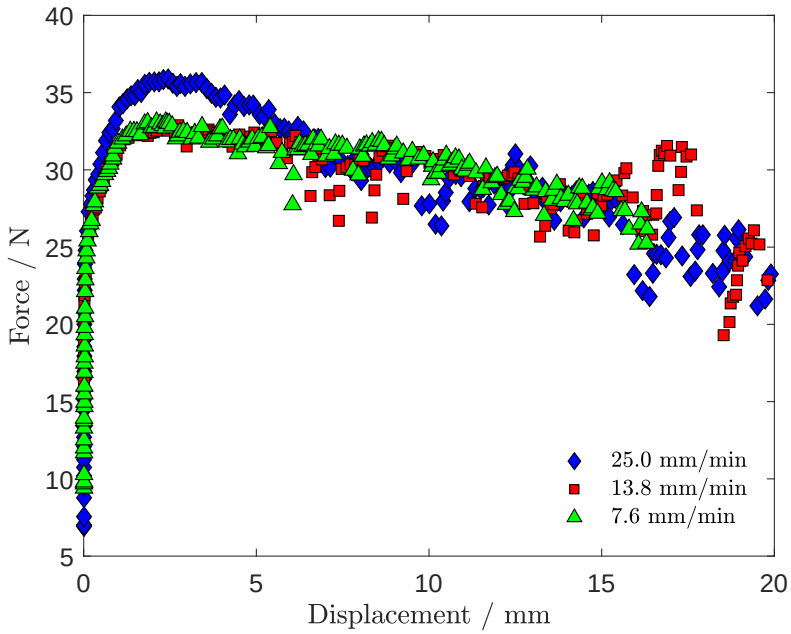

Figure 9: *Force to lift plate (Item 1 Fig. 5) plotted against plate displacement for type B ballotini, with a range of lift speeds. [Fan [6]].*

5.2 Effect of wall friction between the ballotini and the two glass walls

Fan [6] and Teh [27] measured the magnitude of the friction between the ballotini and the two glass retaining walls. This was done by measuring the uplift force during the lifting and lowering of a plate with length 24 mm front to back and of width equal to that of the bed. In this case there would be no slip surface between ballotini particles. Thus the resulting forces were entirely due to the weight of the bed and the friction between particles and the walls. They estimated the coefficient of friction between the ballotini and the wall as $\mu_w \approx 0.4$.

5.3 Angle of slip plane

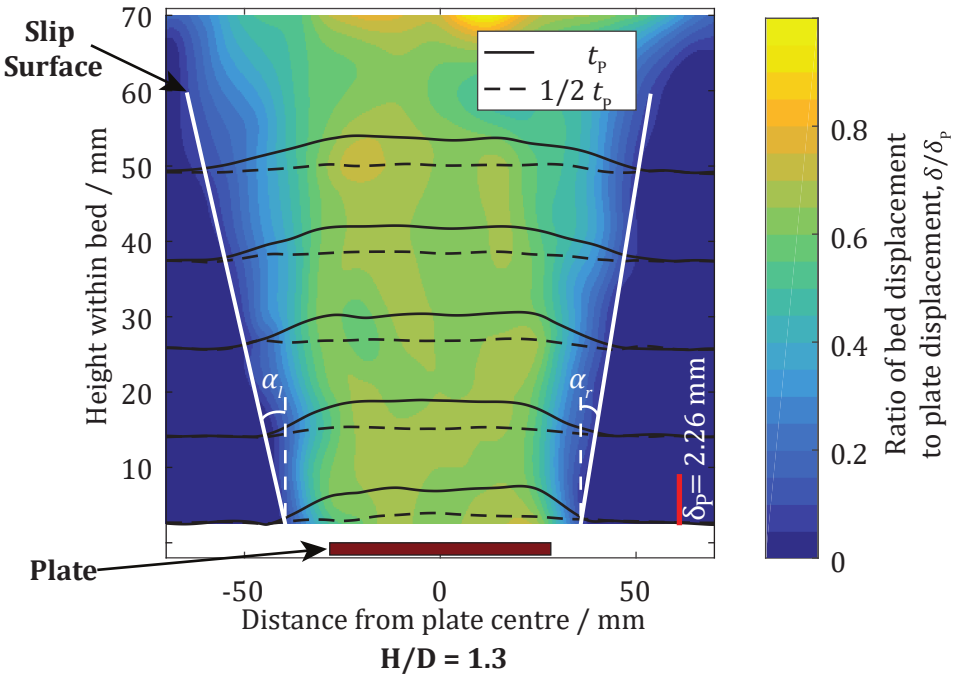

Figure 10: *The coloured map shows the ratio (Ballotini movement)/(Plate movement), δ/δ_p when the peak force is observed (Fig. 9). The particle displacement profiles are shown by the black curves. The continuous curves show the particle displacements at time t_p when the displacement is a maximum (see Fig. 9). The broken curves show the displacements at time $t_p/2$. The positions at which the curves at t_p indicate negligible movement were used to obtain the angle α.*

Fig. 10 shows example results from the particle tracking experiments performed by Fan [6] and Teh [27]. The curves represent the ratio between the bed displacement δ and the plate displacement δ_p. The solid curves represent the ratio of bed displacement to plate displacement δ/δ_p at the time when the lift force is at its maximum, t_p; the broken curves show δ/δ_p at $t_p/2$. The positions as which the displacement profiles at t_p indicate negligible movement were used to obtain α, the angle of the slip plane to the vertical.

Values of α, obtained from the brightness threshold and particle tracking methods, are shown in Fig. 11. The error bars show the estimated measurement uncertainty (see the uncertainty analysis in Section S.1 in the Supplementary Material).

Equation (12) predicts α from first principles, for given values of K, μ and H/D. The friction angle ϕ is assumed to be 30° for the free flowing ballotini; thus $K = 3$ and $\mu = \tan\phi = 0.577$. These values were used in Equation (12) to give the curve shown in Fig. 11. The agreement between theory and experiment is reasonable for $2 < H/D < 4$, but less good for lower values of H/D.

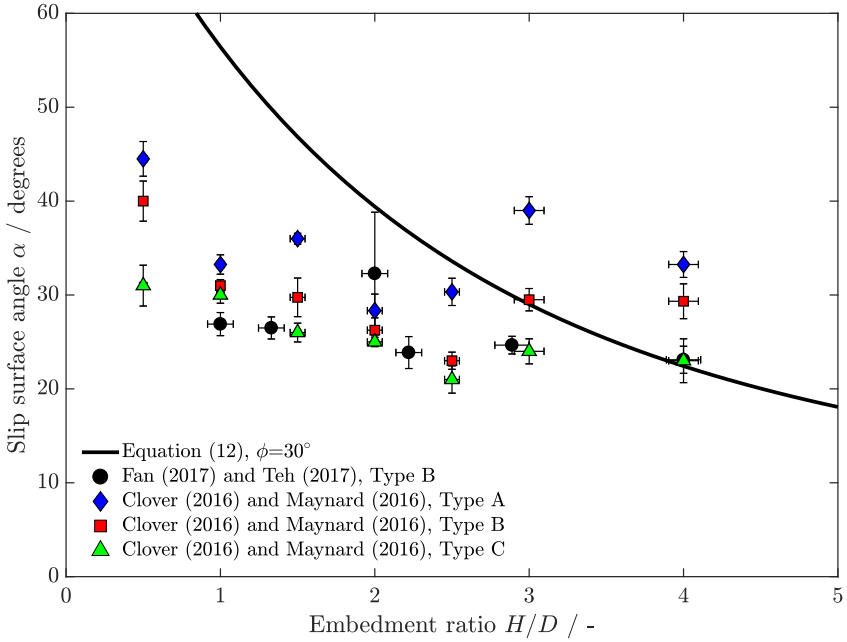

Figure 11: *Angle α between the slip plane and the vertical (see Figs. 3 and 4) for upward moving granular material. The figure shows experimental data from two methods. (i) The brightness threshold method (Clover [3], Maynard [14]). A sample result is shown in Fig. 8. (ii) The particle tracking method (Fan [6], Teh [27]). The error bars show the estimated measurement uncertainty (see the Supplementary Material). The theoretical curve is from Equation* (12) *with K = 3, $\mu = \tan\phi = 0.577$.*

5.4 Breakout factor

Fig. 12 shows data from the experimental work of Clover [3], Maynard [14], Fan [6] and Teh [27]. The error bars show the estimated measurement uncertainty (see Section S.2 in the Supplementary Material). The solid black line shows the theoretical curve from Equation (4) using the value of α predicted by Equation (12). Also shown are the combined contributions of Equation (4) and the wall friction estimated using Equation (17) for the plate widths used in the experiments. The dashed lines show the combined contributions evaluated using the value of α predicted by Equation (12). The grey shaded region shows the locus of combined contributions evaluated using the maximum and minimum experimentally determined values of α at each H/D from Figure 11. It is apparent that the friction between the ballotini and the walls of the equipment is responsible for a significant contribution to the observed breakout factor.

It appears that the trend of results, i.e the relation between N_{qf} and H/D is reasonably well predicted by Equations (4), (12) and (17), in particular the rise of N_{qf} at small $H/D$and the values of N_{qf} at large H/D. The agreement is significantly improved when using experimentally determined values of α instead of Equation (12), demonstrating that the least satisfactory part of the theory relates to the description of the failure surface.

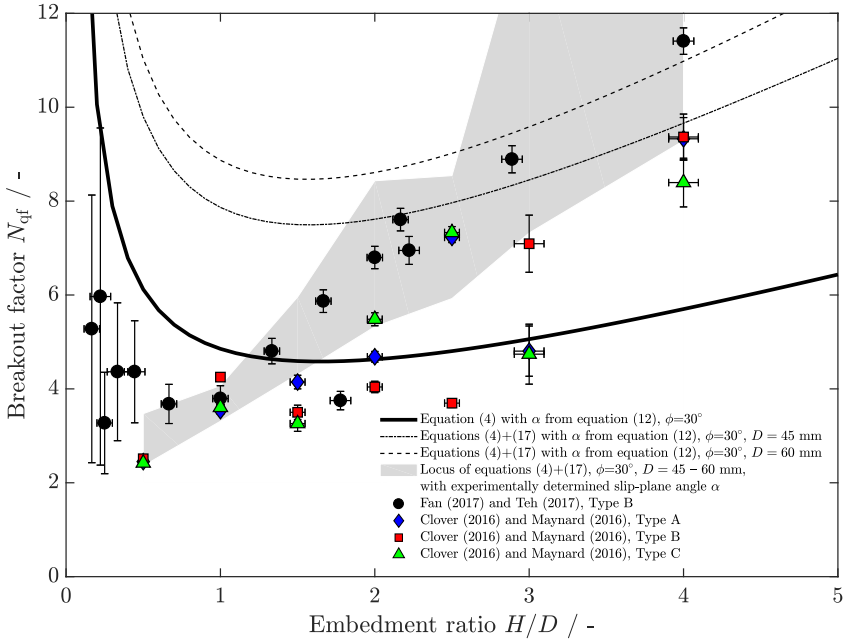

Figure 12: *Breakout factor $N_{qf} = F_T/\rho gHDw$ plotted against H/D. Experimental data compared with theory. The error bars show the estimated measurement uncertainty (see the Supplementary Material).*

5.5 Passive or active motion

The particle tracking method was used to determine whether each element of granular material underwent passive or active motion. Sets of initially square arrays of granular material were considered. The distortion of these arrays at time t_p was inferred by interpolating the displacement of the vertices from the observed displacements of the black ballotini (which were randomly distributed in the bed with sufficient concentration to resolve the motion of the granular material without Nyquist sampling problems). The subsequent motion caused the square arrays to become rectangular, see Fig. 13. The direction of distortion indicates whether motion was active or passive.

It is clear, from Fig. 13, that the central region is in active failure; each element gets longer in the horizontal direction, shorter in the vertical direction. By contrast, the motion of particles in the region of the 'failure surface', marked in Fig. 13 by broken red lines, is clearly passive. The aspect ratio of the particles outside the failure zone remains unchanged, indicating no failure. This is consistent with the theoretical analysis, where the primary assumption is active motion in the moving region of the central core, with the further assumption of passive motion within the 'failure surface' for the purpose of calculating the lift force, and isotropic behaviour in the region outside the 'failure surface' for the purpose of calculating the angle of the slip planes.

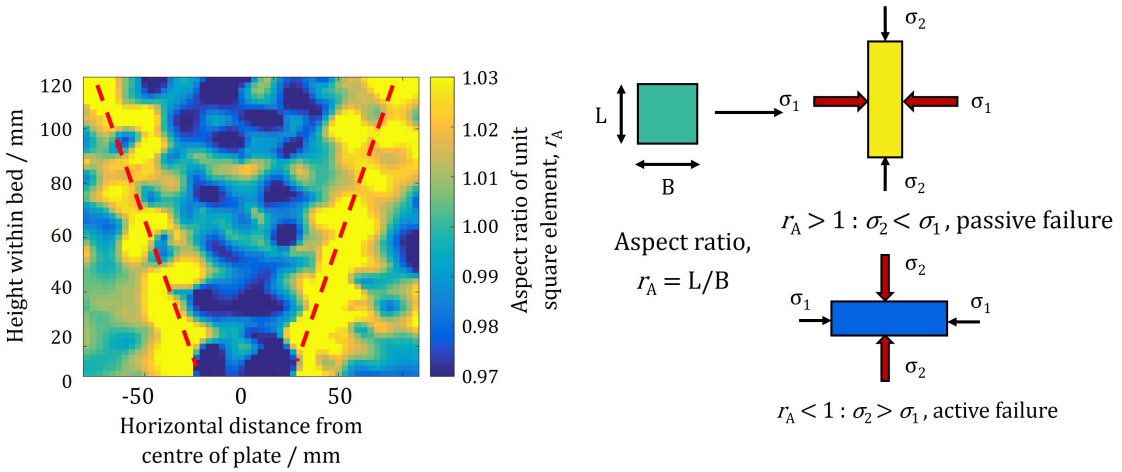

Figure 13: *Passive or active failure? The aspect ratios of a set of initially square arrays of material were was inferred at time t_p by particle tracking. The direction of distortion indicates whether motion was active or passive (Teh [27]).*

6 Conclusions

When a horizontal flat plate immersed in glass ballotini is lifted, a body of ballotini above the plate is also lifted; the body is of 'conical' form, assumed to be bounded by two failure surfaces inclined at angle α to the vertical. Values of α were observed through one of the two vertical parallel glass sheets containing the particles, giving 'two-dimensional' motion. There were two methods:

(1) Image contrast to observe particles with more than a small threshold movement. The photographs suggest two well defined failure lines, giving a plausible measure of α [Clover [3] & Maynard [14]].

(2) Particle tracking, by observation of single particle movements, showed radial upward motion, centred on a point below the lift plate. Particle movements were plotted along horizontal lines above the lift plate, giving a movement profile. Each profile was flat near the centre line, consistent with uniform upward movement. But near the failure surfaces, the movement gradually diminished with distance from the centre-line, falling to zero in the region of the failure surface identified by the image contrast method, (1) above. Thus the particle tracking method suggests that there is no clearly defined 'failure surface'.

The movements of particles, initially in the array of a small square, showed that failure was 'active' near the centre line; but towards the region of the failure surfaces, stresses became either 'isotropic', i.e. equal stress all round an element, or 'passive' i.e. vertical stress less than horizontal stress. These findings formed the basis of theory which assumes 'reverse hopper' flow: the particles near the centre line were assumed to be in 'active' mode i.e. vertical stress greater than horizontal stress. This is the reverse of what

happens in downward hopper flow where the downward moving elements are in passive failure. For the upflow case, the subject of this paper, it is assumed that there are two failure surfaces, inclined at $\pm\alpha$ to the vertical. Between these failure surfaces, it is assumed that failure is active. Outside the two failure surfaces, the forces are assumed to be isotropic, i.e. vertical stress = horizontal stress. This theory, obviously a very simplified representation of reality, does give reasonably good predictions of lift force; the theory also gives fairly good predictions of the measured failure angle $\pm\alpha$, bearing in mind that the data are very scattered, not surprising in view of the above mentioned fact that there is not a well-defined failure surface.

Acknowledgements

This work was partly funded by the National Research Foundation (NRF), Prime Minister's Office, Singapore under its Campus for Research Excellence and Technological Enterprise (CREATE) programme.

Nomenclature

Roman symbols

B	Width of lift plate	m
D	Width of lift plate	m
E	Young modulus	$kgm^{-1}s^{-2}$
F	Lift force	N
F_w	Force due to friction between granules and walls of experimental apparatus	N
F_T	Peak lift force	N
g	Acceleration of gravity	ms^{-2}
H	Bed height	m
K	Rankine coefficient of earth pressure	-
K_f	Rankine coefficient at the failure surface	-
L	Width of element	m
N	Lift force	N
N_{qf}	Dimensionless peak lift force, $N_{qf} = F_T/\rho gHDw$	-
N_{qf_w}	Contribution to observed N_{qf} due to F_w	-
r	Radius from apex of failure surfaces	m
r_A	Aspect ratio, $r_A = L/B$	-
r_0	Radius to edges of lift plate	m
r_1	Radius to top of particle bed	m
t_p	Time when lift force is a maximum	s
w	Distance between vertical glass retaining plates	m
x	Coordinate along slip plane	m
y	Coordinate normal to slip plane	m

Greek symbols

α	Angle between the slip plane and the vertical	rad
δ	Bed displacement	m
δ_p	Lift plate displacement	m
ε_w	Strain perpendicular to the wall	-
ζ	Substitution for $1 + \frac{2H\tan\alpha}{D}$	-
μ	Internal friction coefficient of granules	-
μ_w	Coefficient of friction between granules and walls of experimental apparatus	-
ν	Poisson ratio	-
ρ	Bulk density of particle bed	kgm^{-3}
σ	Stress in granular material	Nm^{-2}
σ_1	Principal stress within flowing granular material	Nm^{-2}
σ_2	Principal stress within flowing granular material	Nm^{-2}
σ_3	Stress parallel to failure surface in granular material	Nm^{-2}

σ_4	Stress normal to failure surface in granular material	Nm^{-2}
σ_w	Normal stress on walls of experimental apparatus	Nm^{-2}
τ	Shear stress on wall element	Nm^{-2}
ϕ	Internal friction angle of granules	rad

Abbreviations

PTVA	Particle tracking velocity algorithm

Supplementary Material

Uncertainty analysis

S.1 Angle of slip plane

S.1.1 Brightness threshold method

The main uncertainty in the estimation of the angle of the slip plane comes from the identification of the interface between the moving and stationary material. This is illustrated in Fig. S.1, which shows upper and lower estimates of the angle, α on both sides of the diagram. The upper limit shown by the error bars on the brightness threshold data in Fig. 11 show the maximum of α_{U1} and α_{U2} for each experiment. Likewise, the lower limit shown by the errors bars shows the minimum of α_{L1} and α_{L2} for each experiment.

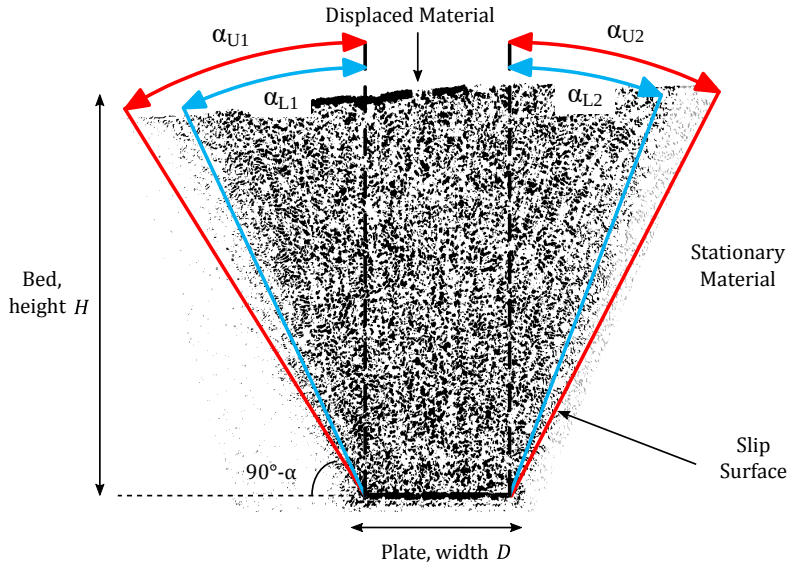

Figure S.1: *Example output from the brightness threshold method. The red and blue lines show perceived upper and lower bounds on estimates of the angle* α.

S.1.2 Particle tracking method

The particle tracking method uses a displacement threshold δ/δ_p, defined as the ratio of particle movement to plate displacement, to identify quantitatively α, the angle of the slip plane between the moving and stationary material. It is necessary to specify the displacement threshold as a range in order identify a large enough region of material to define a clear interface. However, the location of the interface and hence the value of the angle α depends on the chosen value of the displacement threshold. This is illustrated in Fig. S.2.

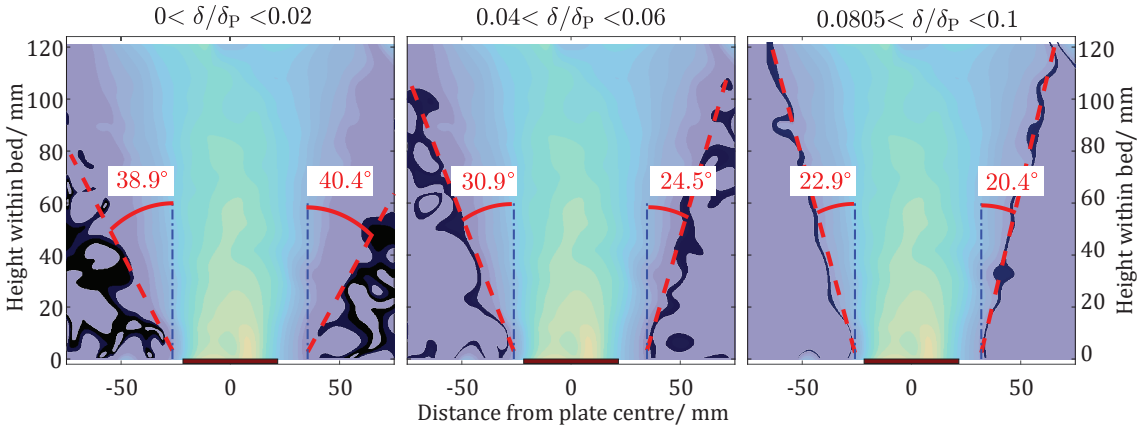

Figure S.2: *Example output from the particle tracking method. Each panel shows the same image analysed using a different displacement threshold, δ/δ_p. The angle α depends on the displacement threshold and varies between the left hand and right hand sides of the image.*

The angles reported in Fig. 11 were measured using a displacement threshold in the range $0.02 \leq \delta/\delta_p \leq 0.05$. This is the smallest range of displacements that enabled the reliable identification of an interface. Typically, no defined slip surface could be found for displacement thresholds $\delta/\delta_p \leq 0.02$. The errors in the angles estimated from the left and right hand sides of the images, $\Delta\alpha_L$ and $\Delta\alpha_R$, are estimated as the standard error (SE) of each set repeat measurements

$$\mathrm{SE} = \frac{s_{n-1}}{\sqrt{n}},$$

where s_{n-1} is the bias-corrected standard deviation of the measurements and n is the number of repeats. The error bars on the particle tracking data in Fig. 11 show the mean error

$$\Delta\alpha = \frac{1}{2}\left(\Delta\alpha_L + \Delta\alpha_R\right). \tag{S.1}$$

S.2 Breakout factor

The main uncertainties in the measurement of the breakout factor

$$N_{qf} = \frac{F_T}{\rho g H D w},$$

and the embedment ratio are assumed to be the measurement of the peak force F_T, the bulk density ρ and the bed height H. The plate was machined to high precision, so the errors in its length D and width w are assumed to be negligible.

- The uncertainty in the peak force is estimated as

$$\Delta F_T = \sqrt{\Delta F_1^2 + \Delta F_2^2}, \tag{S.2}$$

where F_1 is the lift force measured in experiments with ballotini, F_2 is the lift force measured in experiments without ballotini (so F_2 is the weight of the rod plus any contribution from friction in the equipment) and where the peak force is calculated as $F_T = F_1 - F_2$. The values of ΔF_1 and ΔF_2 are estimated as the standard error (SE) of each set repeat measurements

$$\mathrm{SE} = \frac{s_{n-1}}{\sqrt{n}},$$

where s_{n-1} is the bias-corrected standard deviation of the measurements and n is the number of repeats.

- The uncertainty in bulk density $\Delta\rho$, was taken as ± 20 kg m^{-3} based on the experimental measurements of Reci [24] and Lao [9].
- The uncertainty in the bed height ΔH was primarily due to the difficulty in levelling the top of the bed and was estimated as ± 5 mm.

The overall uncertainty in the breakout factor is calculated as

$$\begin{aligned}\Delta N_{\mathrm{qf}} &= \sqrt{\left(\Delta F_T \frac{\partial N_{\mathrm{qf}}}{\partial F_T}\right)^2 + \left(\Delta\rho \frac{\partial N_{\mathrm{qf}}}{\partial \rho}\right)^2 + \left(\Delta H \frac{\partial N_{\mathrm{qf}}}{\partial H}\right)^2}, \\ &= \sqrt{\left(\frac{\Delta F_T}{\rho g H D w}\right)^2 + \left(\frac{\Delta\rho\ F_T}{\rho^2 g H D w}\right)^2 + \left(\frac{\Delta H\ F_T}{\rho g H^2 D w}\right)^2}, \end{aligned} \tag{S.3}$$

and in the embedment ratio

$$\Delta\left(\frac{H}{D}\right) = \frac{\Delta H}{D}. \tag{S.4}$$

References

[1] A. Balla. The resistance to breaking out of mushroom foundations for pylons. In Proceedings of the 5th International Conference on Soil Mechanics and Foundation Engineering, volume 1, pages 569–576, Paris, France, 1961.

[2] C. Y. Cheuk, D. J. White, and M. D. Bolton. Uplift mechanisms of pipes buried in sand. Journal of Geotechnical and Geoenvironmental Engineering, 134(2):154–163, 2008. doi:10.1061/(ASCE)1090-0241(2008)134:2(154).

[3] M. Clover. Uplift mechanism for an object buried in granular material. Master's thesis, University of Cambridge, Department of Chemical Engineering and Biotechnology, 2016.

[4] E. A. Dickin. Uplift behavior of horizontal anchor plates in sand. Journal of Geotechnical Engineering, 114(11):1300–1317, 1988. doi:10.1061/(ASCE)0733-9410(1988)114:11(1300).

[5] E. A. Dickin. Uplift resistance of buried pipelines in sand. Soils and Foundations, 34(2):41–48, 1994. doi:10.3208/sandf1972.34.2_41.

[6] R. A. Fan. Uplift mechanism of granular material by a horizontal plate. Master's thesis, University of Cambridge, Department of Chemical Engineering and Biotechnology, 2017.

[7] A. Ghaly, A. Hanna, and M. Hanna. Uplift behavior of screw anchors in sand. i: Dry sand. Journal of Geotechnical Engineering, 117(5):773–793, 1991. doi:10.1061/(ASCE)0733-9410(1991)117:5(773).

[8] K. Ilamparuthi, E. A. Dickin, and K. Muthukrisnaiah. Experimental investigation of the uplift behaviour of circular plate anchors embedded in sand. Canadian Geotechnical Journal, 39(3):648–664, 2002. doi:10.1139/t02-005.

[9] C. Lao. Uplift mechanism for an object buried in granular material. Master's thesis, University of Cambridge, Department of Chemical Engineering and Biotechnology, 2015.

[10] K. F. Lee, J. F. Davidson, J. Akroyd, and M. Kraft. Lifting a buried object: Reverse hopper theory. Chemical Engineering Science, 105:198 – 207, 2014. ISSN 0009-2509. doi:10.1016/j.ces.2013.11.002.

[11] H. MacDonald. Uplift Resistance of Caisson Piles in Sand. Nova Scotia Technical College, 1963. URL https://books.google.co.uk/books?id=5m9CNwAACAAJ.

[12] J. Majer. Zur berechnung von zugfundamenten. Osterreichische Bauzeitgschrift, 10 (5):85–90, 1955.

[13] E. L. Matyas and J. B. Davis. Prediction of vertical earth loads on rigid pipes. Journal of Geotechnical Engineering, 109(2):190–201, 1983. doi:10.1061/(ASCE)0733-9410(1983)109:2(190).

[14] O. Maynard. Uplift mechanism for an object buried in granular material. Master's thesis, University of Cambridge, Department of Chemical Engineering and Biotechnology, 2016.

[15] R. S. Merifield and S. W. Sloan. The ultimate pullout capacity of anchors in frictional soils. Canadian Geotechnical Journal, 43(8):852–868, 2006. doi:10.1139/T06-052.

[16] R. S. Merifield, A. Pearce, H. S. Yu, and S. W. Sloan. Stability of anchor plates. In Proceedings 8th Australia New Zealand Conference on Geomechanics: Consolidating Knowledge, pages 553–560, 1999.

[17] M. Moradi and W. Craig. Observation of upheaval buckling of buried pipelines. Centrifuge, 98:693–698, 1998.

[18] H. Mors. The behaviour of mast foundations subject to tensile forces. Bautechnik, 10:367–378, 1959.

[19] E. J. Murray and J. D. Geddes. Uplift of anchor plates in sand. Journal of Geotechnical Engineering, 113(3):202–215, 1987. doi:10.1061/(ASCE)0733-9410(1987)113:3(202).

[20] R. M. Nedderman. Statics and Kinematics of Granular Materials, chapter 3, page 25. Cambridge University Press, 1992.

[21] C. Ng and S. Springman. Uplift resistance of buried pipelines in granular material. International Conference Centrifuge, 94:753–758, 1994.

[22] B. C. Punmia, A. K. Jain, and A. K. Jain. Soil Mechanics and Foundations. Laxmi Publications, New Delhi, India, 16 edition, 2005.

[23] K. S. S. Rao and J. Kumar. Vertical uplift capacity of horizontal anchors. Journal of Geotechnical Engineering, 120(7):1134–1147, 1994. doi:10.1061/(ASCE)0733-9410(1994)120:7(1134).

[24] A. Reci. The physics of lifting an object buried in granular material. Master's thesis, University of Cambridge, Department of Chemical Engineering and Biotechnology, 2015.

[25] R. K. Rowe and E. H. Davis. The behaviour of anchor plates in clay. Géotechnique, 32(1):9–23, 1982. doi:10.1680/geot.1982.32.1.9.

[26] K. Stone and T. A. Newson. Uplift resistance of buried pipelines. Proceedings of 6th International Conference on Physical Modelling in Geotechnics, 1:741–746, 2006.

[27] K. K. Teh. Uplift mechanism for a horizontal anchor buried in granular material. Master's thesis, University of Cambridge, Department of Chemical Engineering and Biotechnology, 2017.

[28] C. H. Trautmann, T. D. O'Rourfce, and F. H. Kulhawy. Uplift force-displacement response of buried pipe. Journal of Geotechnical Engineering, 111(9):1061–1076, 1985. doi:10.1061/(ASCE)0733-9410(1985)111:9(1061).

[29] P. A. Vermeer and W. Sutjiadi. The uplift resistance of shallow embedded anchors. Proceedings of 11th International conference on Soil Mechanics and Foundation Engineering, 3:1635–1638, 1985.

[30] D. J. White, W. A. Take, and M. D. Bolton. Soil deformation measurement using particle image velocimetry (piv) and photogrammetry. Géotechnique, 53(7):619–631, 2003. doi:10.1680/geot.2003.53.7.619.

[31] D. J. White, C. Y. Cheuk, , and M. D. Bolton. The uplift resistance of pipes and plate anchors buried in sand. Géotechnique, 58(10):771–779, 2008. doi:10.1680/geot.2008.3692.